Shock wave propagation along the central retinal blood vessels

T. A. Spelman* & P. S. Stewart*

January 16, 2020

Abstract

Retinal haemorrhage is often observed following brain injury. The retinal circulation is supplied (drained) by the central retinal artery (vein) which enters (leaves) the eye through the optic nerve at the optic disc; these vessels penetrate the nerve immediately after passing through a region of cerebrospinal fluid (CSF). We consider a theoretical model for the blood flow in the central retinal vessels, treating each as multi-region collapsible tubes, where we examine how a sudden change in CSF pressure (mimicking an injury) drives a large amplitude pressure perturbation towards the eye. In some cases this wave can steepen to form a shock. We show that the region immediately proximal to the eye (within the optic nerve where the vessels are strongly confined by the nerve fibres) can significantly reduce the amplitude of the pressure wave transmitted into the eye. When the length of this region is consistent with clinical measurements, the CSF pressure perturbation generates a wave of significantly lower amplitude than the input, protecting the eye from damage. We construct an analytical framework to explain this observation, showing that repeated rapid propagation and reflection of waves along the confined section of the vessel distributes the perturbation over a longer lengthscale.

1 Introduction

Retinal haemorrhage (bleeding of the retinal blood vessels) can be triggered by a traumatic brain injury [1]; haemorrhages can be classified into different types depending on their depth and location and are often used clinically to track the progress of an injury. Retinal haemorrhaging is also one of the clinical identifiers of 'Shaken Baby Syndrome' [2].

Predicting the onset of retinal haemorrhage, and how it correlates to the severity of brain injury, is an important open question, particularly in legal cases of suspected non-accidental injury in infants where the circumstances may be subject to dispute [3, 4].

There are a number of mechanisms thought to drive retinal haemorrhage following head trauma. This study focuses on the response of the eye to an acute rise in cerebrospinal fluid (CSF) pressure in the brain (this pressure is also known as the intracranial pressure, ICP), where haemorrhage is attributed to the rupture of one or more retinal vessels following the accompanying rise in intraocular venous pressure [5]. We propose a theoretical model to examine how acute

*School of Mathematics and Statistics, The Mathematics and Statistics Building, University Place, University of Glasgow, Glasgow, UK. G12 8SQ

changes in ICP can result in large amplitude elastic jumps (shock waves) propagating along the retinal vessels into the eye. Vitreoretinal traction is also believed to lead to retinal haemorrhage, where rapid acceleration/deceleration of the skull (*eg.* shaking) can lead to shearing forces between the vitreous and the retina, which can in turn contribute to rupture of blood vessels close to the surface [6, 7]. These extra features have not been considered here for simplicity.

This study builds on our earlier work examining the origins of bleeding along the optic nerve (the tissue which connects the eye to the brain) following traumatic brain injury. In that work we used a theoretical model to simulate the flow of cerebrospinal fluid (CSF) along the optic nerve sheath in response to an acute rise in intracranial pressure mimicking an injury: we showed how a steepening pressure wave can propagate along the sheath toward the eye and be reflected back by the (relatively) impermeable sclera. Interestingly, this reflection can lead to significant amplification of the CSF pressure close to the sclera [8].

During foetal development the eyes originate from within the developing brain. As the eyes develop they become confined within a bony structure known as the orbit, but remain connected to the brain by the optic nerve, a dense collection of nerve fibres connecting the light sensitive cells in the retina to the thalamus in the brain. The optic nerve is confined by a sheath containing a thin layer of CSF (at the intracranial pressure) while the eye itself is filled with vitreous at the intraocular pressure. In this study we consider blood flow in the central retinal vessels, the central retinal artery (CRA) and the central retinal vein (CRV), which pass along the centre of the optic nerve before entering the eye at the optic disc and branching into the retinal circulation. The geometry of these vessels has been well described by Hayreh and others [9–11] and is sketched in Fig. 1(a). However, these vessels do not follow the course of the nerve entirely, but instead turn and pass through the nerve sheath into the extra-neural space about a centimetre back from the eye. Hence, these central retinal blood vessels are externally exposed to the CSF pressure as they cross the nerve sheath. Our hypothesis is that an acute rise in CSF pressure in the nerve sheath will be transmitted externally to the central retinal vessels, driving blood flow into the retinal circulation and leading to a corresponding increase in blood pressure. This increase in blood pressure could then lead to vessel bursting (retinal haemorrhage), particularly on the venous side where the vessels are typically weaker. We assume that our system is relatively isolated from the other extreme events that will occur following traumatic brain injury (such as compressible shock waves propagating in a complicated media comprised of skull, CSF, parenchyma, blood vessels *etc*), coupled only to the abrupt rise in the CSF pressure which is within the optic nerve sheath and external to the central retinal vessels.

To construct a theoretical model for this pressure transmission we treat each vessel as a long collapsible tube formed by multiple regions in series, where each region represents a different external pressure environment. This approach is similar to our previous work to understand the onset of retinal venous pulsation [12, 13], where we were able to deduce a threshold for the onset of large amplitude oscillations in blood pressure as a function of the (relatively normal) pressures in the eye and the brain. However, the acute CSF pressure increases considered in this study will be of significantly larger amplitude (and on a vastly different timescale) to normal CSF pressure fluctuations in the brain. This increases the likelihood of additional, potentially harmful, characteristics such as wave steepening and formation of shock fronts (often termed elastic jumps in the context of elastic-walled tubes). Propagating elastic jumps in single vessels have been studied both analytically [14] and numerically using a specially adapted solver [15], although there is a much greater body of work on the closely related system of shock waves in (compressible) gas dynamics (eg [16, 17]).

The model constructed within this paper is a specific example of a more general class of problems involving large-amplitude waves propagating through media with inhomogeneous geometric or material properties. For example, recent work has considered flow through a collapsible tube with discontinuous material properties showing the coexistence of multiple steady states when the flow is supercritical [18, 19]. Furthermore, similar ideas have been considered in the gas dynamics literature with shock waves propagating through a pipe with a section of expanded cross-sectional area [20, 21] with application to exhaust systems.

This paper is arranged as follows. In Sec. 2 we introduce the model equations and baseline parameters along with the analytical and numerical methods used to solve our system. In Sec. 3 we discuss the blood vessel response to an acute rise in CSF pressure.

2 The models

We study the flow along the CRA and CRV in response to a traumatic increase in CSF pressure. We model the blood vessel geometry as a four region system shown in Fig. 1(a). In describing the model we will not distinguish explicitly between the artery and vein but instead consider a generic blood vessel. However, we will specify to the CRA or CRV through particular material and geometric parameters (listed in Table 1).

In this study we assume the pressure perturbations applied externally to the vessel are of such large amplitude that the relatively small viscous pressure drop along the vessel can be ignored in comparison. These pressure drops are estimated in the supplementary material. Hence, we model the blood as an inviscid fluid of fixed density ρ^*.

We model the path of the blood vessel using a four region model, shown in Fig. 1(b), where each portion is modelled as a one-dimensional collapsible tube parametrised by the coordinate x^* oriented along its axis and time t^*. We characterise the tube by its local cross-sectional area, $A^*(x^*, t^*)$, the corresponding flux of blood along the axis, $q^*(x^*, t^*)$ and the blood pressure, $p^*(x^*, t^*)$.

In this inviscid model we assume that the baseline cross-sectional area of the tube is constant, denoted A_0^* (ignoring the influence of vessel tapering), and that the baseline flux of blood is negligible in comparison to those induced by the pressure perturbation. The latter is reasonable as we expect much larger fluxes to be generated by the pressure forcing: typical retinal blood flow is $\approx 44\mu$l/min [22], while in the example discussed in Sec. 33.1 the model predicts a much greater maximal flux of $\approx 190\mu$l/min. Our neglect of a base flow means that the flow system is always subcritical and so precludes phenomena such as 'choking' [23] and multiple co-existing flow states [19].

We consider a baseline pressure p_0^* and assume the external pressure is initially spatially uniform and equal to this baseline value (for simplicity). In reality the pressure surrounding the region of the vessel in the eye is $\approx$ 10mmHg larger that that in the CSF, but again this difference is small compared to the traumatic pressure perturbations applied below. The influence of this pressure drop is explored in the supplementary material, where is made no significant difference to the predictions.

The governing equations follow from the Euler equations of conservation of mass and momentum for an inviscid fluid in the limit of long-wavelength disturbances [24]. As in previous models, in regions where the vessel is flexible an extra condition is required to close the model equations, which follows from a balance of stress across the tube wall. In this model the wall flexibility

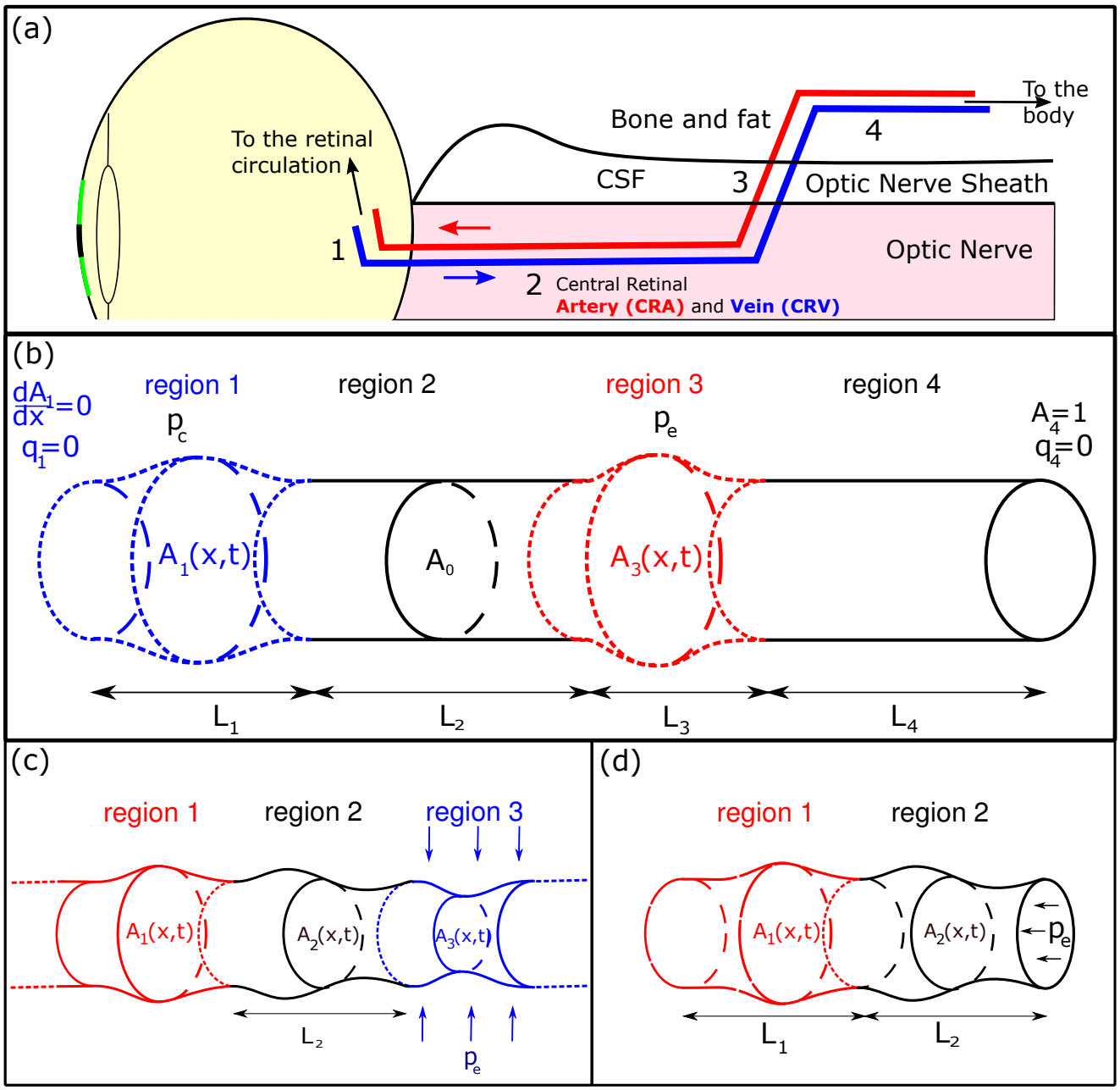

Figure 1: Setup of the theoretical models: (a) sketch of the optic nerve and eye including the CRV and CRA; (b) setup of the full four region model for an individual blood vessel; (c) simplified setup used to build an analytical model in Sec. 22.4; (d) further simplified setup used to analyse the energy distribution in Sec. 33.4. Parameters are defined in Table 2.

is characterised by two parameters in each region ($j = 1, \cdots, 4$), a resistance to expansion or compression, denoted k_j^*, and an axial membrane tension, denoted Γ_j^* (similar to many previous modelling studies *eg.* blood vessels [25] and airways [26]).

In region 1, of length L_1^* spanning $-L_1^* \leq x^* \leq 0$, the vessel is within the eye itself and externally surrounded by vitreous at the intraocular pressure. The vessel is able to expand and

change shape (especially the central retinal vein, with large amplitude oscillations evident as the retinal venous pulse [12]); the external pressure on this region assumed to be $p_c^* = p_0^*$ throughout the main text (the influence of a raised intraocular pressure compared to the intracranial pressure is explored in the supplementary material). Similarly, in region 3, of length L_3^* spanning $L_2^* \leq x^* \leq L_2^* + L_3^*$, the vessel bridges the optic nerve sheath and so externally surrounded by CSF, and so can expand or compress in response to changes in external CSF pressure $p_e^*(t)$ (such that $p_e^*(0) = p_0^*$), which are prescribed in the present model. Dynamic changes in CSF pressure following a traumatic pressure perturbation in the brain were described in our previous study [8].

The intermediate region through the centre of the optic nerve, designated region 2 of length L_2^* spanning $0 \leq x^* \leq L_2^*$, is key to the results presented below. The vessel will be tightly confined by the surrounding nerve fibres as it passes through this region [27] and so unable to deform as freely as regions 1 and 3. For simplicity, in most of this study we assume the vessel is entirely rigid across region 2. (However, in Sec. 22.4 and Sec. 33.4 we consider a simplified version of our system which treats this region as flexible but more restricted in expansion compared to regions 1 and 3.) Compartment 4, of length L_4^* spanning $L_2^* + L_3^* \leq x^* \leq L_2^* + L_3^* + L_4^*$, where the vessel is passing through the extra nerve space, has limited influence on the behaviour and is treated as rigid for simplicity. In the reduced models presented below this region is ignored with little or no effect on the results.

In each region we label the dependent variables (A_j^*, q_j^*, p_j^*) and the region specific parameters (k_j^*, Γ_j^*) with the subscript j ($j = 1, \cdots, 4$).

This model contains an idealised representation of flow in the central retinal vessels. However, it also forms a model system for studying the transmission of a localised external pressure increase across a flexible-walled vessel, and a model problem for propagation of shock waves through inhomogeneous domains.

2.1 Parameter choices

The baseline values we use for the dimensional parameters are detailed in Tables 1 and 2.

The vessel stiffness parameter k_j^* ($j = 1, \cdots, 4$) presents the most uncertainty due to inconsistent experimental measurements. When non-dimensionaling the system below we consider a baseline value in region 3 (*ie* k_3^*) and calculate this parameter (measuring the resistance to expansion or compression) from the Youngs modulus of the tissue, denoted E^*, its Poisson ratio ν, the wall thickness h^* and inner lumen radius r_0^* in the form, [28]

$$k_3^* = \frac{E^*}{12(1-\nu^2)^{1/2}} \left(\frac{h^*}{r_0^*}\right)^3, \tag{1}$$

assuming the material is a linearly elastic thin shell. We assume that the tissue is approximately incompressible ($\nu = 0.49$). In principle, the Youngs modulus of the tissue can be inferred (approximately) from experimental measurements of the Pulse Wave Velocity (PWV) within human retinal blood vessels, which has been correlated to the linear theory of pulse propagation in blood vessels through the Moens–Korteweg equation [29]. However, PWV measurements in retinal arteries span a wide range, including $4 \times 10^{-4}\,\mathrm{ms}^{-1}$ [31,32], 0.01-0.03 ms^{-1} [33,34] and $0.6\,\mathrm{ms}^{-1}$ [36]. The inconsistencies between these results is discussed by [37] and it is unlikely that such variability is seen between patients. Due to these issues, we take $E^* = 0.3\,\mathrm{MPa}$ in the artery and $E^* = 0.6\,\mathrm{MPa}$ in the vein, as a baseline value of the Youngs modulus; these values have previously been used to produce models of the retinal circulation [41] and are of comparable magnitude to

the Youngs modulus of similarly sized blood vessels elsewhere in the body [38, 39]. However, due to the uncertainty in E^* we will examine the effect of varying E^* in Sec. 33.3 below.

We note that in this model the membrane tension parameter, Γ_j^* $(j = 1, \cdots, 4)$, is used to increase the order of spatial derivatives in the model from two to four and allow us to enforce two additional boundary conditions. We expect this term to be small across most of the vessel when compared to the contribution of the tube law. In simulations below we set $\Gamma_j^* = \Gamma^*$ $(j = 1, \cdots, 4)$, where the value of Γ^* is taken to be small. We note that inclusion of this additional term leads to dispersive waves around the advancing wavefront whose wavelength scales with the size of Γ^*. We explore the influence of this parameter on the model predictions in the supplementary material, showing that the behaviour of the system is qualitatively very similar to the simulations reported here provided $\Gamma \leq 10^{-3}$. For larger choices of the tension parameter the generated pressure perturbation in region 1 is typically spread over the entire domain (not localised into a sharp gradient).

We approximate the baseline external pressure on the vessels p_0^* as the orbital tissue pressure, measured in the range $\lesssim 2.6$mmHg [35].

The system is forced by an external pressure perturbation in the CSF surrounding the blood vessel in region 3, modelling an acute pressure rise in the nerve sheath (see our previous study for details [8]). Here we impose the external pressure acting on region 3 as a simple time dependent function in the form

$$p_e^* = \begin{cases} p_0^* + \Delta p^* \sin^2\left(\pi t^*/t_{ap}^*\right) & 0 \leq t^* \leq t_{ap}^* \\ p_0^* & t^* > t_{ap}^* \end{cases}, \tag{2}$$

where Δp^* and t_{ap}^* are the amplitude and timescale of the perturbation, respectively. We consider the range $\Delta p^* \approx 0.1 - 1000$ mmHg and $t_{ap}^* \approx 0.1 - 10\,\text{ms}$, which is comparable to the estimated timescale of contact for free-fall impacts [40].

In the reduced models outlined below (Sec. 22.4) we use a simpler form of $p_e(t)$ to facilitate an analytical model. To effectively compare the approaches we hold the time-integrated $p_e(t)$ constant, denoted

$$I_{tot}^* = \int_0^{t_{ap}^*} (p_e^* - p_0^*)\,\mathrm{d}t^*. \tag{3}$$

For the pressure waveform (2) we obtain $I_{tot}^* = \frac{1}{2}\Delta p^*\, t_{ap}^*$.

It should be noted that this model neglects the influence of auto-regulation in the retinal circulation (see detailed model in [41]) and other mechanisms of vessel active contraction [42], assuming these would only act on longer timescales than those of interest here.

Parameter	Symbol	Artery	Vein
Vessel lumen radius	r_0^*	$87.5\,\mu$m	$119\,\mu$m
Vessel cross-sectional area	$A_{10}^* = A_{30}^* = A_0^*$	2.4×10^{-8} m^2	4.4×10^{-8} m^2
Vessel wall thickness	h^*	$39.7\,\mu$m	$10.7\,\mu$m
Vessel wall Youngs modulus	E^*	0.3 MPa	0.6 MPa
Vessel wall stiffness	$k_1^* = k_3^* = k^*$	2600 Pa	40 Pa

Table 1: Baseline model parameter values specific to the CRA and CRV [41] with the elastic stiffness parameter estimated using (1).

Parameters	Symbol	Value	Citation
Poisson Ratio	ν	0.49	[41]
Density of blood	ρ^*	$10^3\,\mathrm{kgm}^{-3}$	[29]
Membrane tension	Γ^*	$10^{-5} - 10^{-3}$	
Length of region 1	L_1^*	$\approx 10^{-3}\,\mathrm{m}$	[43]
Length of region 2	L_2^*	$\approx 10^{-2}\,\mathrm{m}$	[9]
Length of region 3	L_3^*	$\approx 10^{-3}\,\mathrm{m}$	[44]
Length of region 4	L_4^*	$\approx 10^{-2}\,\mathrm{m}$	[12]
Timescale of perturbation	t_{ap}^*	$0.1 - 10\,\mathrm{ms}$	[40]
Baseline external pressure	p_0^*	2.6mmHg	[35]

Table 2: Reference parameter values applicable to both the CRV and CRA.

2.2 Non-dimensional variables

We non-dimensionalise the Euler equations of mass and momentum conservation by scaling relative to the properties of region 3: so scale all lengths on L_3^*, cross-sectional areas on A_0^*, velocities on $U_0^* = (k_3^*/\rho^*)^{1/2}$, time on $t_0^* = L_3^*/U_0^*$ and pressures according to $p^* = k_3^* p + p_0^*$, where p^* (p) represent the dimensional (dimensionless) pressures. This results in the following dimensionless groups

$$\beta = \frac{A_0^{*1/2}}{L_3^*}, \qquad t_{ap} = \frac{t_{ap}^*}{t_0^*}, \qquad \Delta p = \frac{\Delta p^*}{k_3^*}, \qquad I_{tot} = \frac{I_{tot}^*}{k_3^* t_0^*}, \tag{4a}$$

$$k_j = \frac{k_j^*}{k_3^*}, \qquad \Gamma_j = \frac{\Gamma_j^* A_0^{*1/2}}{k_3 L_3^2}, \qquad L_j = \frac{L_j^*}{L_3^*}, \qquad (j = 1, 2, 3, 4). \tag{4b}$$

Assuming the aspect ratio of the tube is small, $\beta \ll 1$ (*ie* perturbations are long-wavelength) gives (leading-order) non-dimensional mass and momentum governing equations for each region as

$$\frac{\partial A}{\partial t} + \frac{\partial q}{\partial x} = 0, \qquad \frac{\partial q}{\partial t} + \frac{\partial}{\partial x}\left(\frac{q^2}{A}\right) = -A\frac{\partial p}{\partial x}. \tag{5}$$

These long-wavelength equations have been used extensively in physiological fluid mechanics (*eg* [15,19]) and a derivation from the Navier–Stokes equations is given in the supplementary material.

In regions where the vessel wall is elastic (not rigid) we require additional equations to close our system. We here assume the wall can only move normal to the longitudinal axis of the tube and we use a constitutive law for the elastic properties of the wall which follows from a balance of normal stress. In this study, we adopt the form of the constitutive law used by [15], but we also add an axial membrane tension (as in many previous studies on flow in collapsible tubes *eg* [25] assuming linearised curvature in this long-wavelength form), so our constitutive law takes the non-dimensional form

$$p = p_e(t) + k\mathcal{F}(A) - \Gamma\frac{\partial^2 A}{\partial x^2}, \qquad \mathcal{F}(A) = \left[A^m - A^{-n}\right], \tag{6}$$

where the parameters $m, n > 0$. Throughout the main text we choose $m = 10$ and $n = 3/2$ [15] and apply these exponents to both arteries and veins. However, in the supplementary material we consider an alternative tube law for arteries which has $m = 1$ (linear relationship between

cross-sectional area and pressure in expansion) [25]. Thus, the governing equations in all regions where the vessel wall is deformable are Eqs. (5) and (6).

Conversely, if a region is assumed rigid there is no need for an elastic constitutive law. Here we apply (5) with constant cross-sectional area (equal to 1 when non-dimensionalised). Since q is independent of x in this region, we can integrate the momentum equation with respect to x and derive an expression for the pressure along the region as

$$p = -x\frac{\partial q}{\partial t} + P_0, \tag{7}$$

where P_0 is an integration constant. Applying boundary conditions between regions (discussed further below) determines this integration constant and we deduce an ODE constraint which forms a boundary condition for the compliant sections (similar to previous models of collapsible channels *eg* [45, 46]).

At internal junctions between regions we require the fluid flux and pressure to match at the boundary between regions. In the shock capture numerical method (discussed below) we use conservation of static pressure rather than total pressure for simplicity (in contrast to [47]); we validated this approximation by comparing both matching approaches at a region boundary and noticed negligible difference. Furthermore, in cases including membrane tension we also impose continuity of cross-sectional area between regions.

In our model we assume that the base-line flow along the vessel is negligible in comparison to the flow induced by the trauma. This assumption has the significant advantage that arteries and veins can be treated with the same boundary conditions. For consistency with this assumption we then assume no flow into or out of the the domain at the external boundaries, which mimics closing of the (venous) outflow pathways as a result of the injury. In reality the appropriate boundary condition for the retinal artery/vein will be a mixed condition involving both pressure and flux, although the most appropriate formulation to use is unclear. Thus, our no-flux boundary condition is one extreme but we compare the vessel profiles obtained with this condition to the other extreme of enforcing pressure equal to the baseline value ($p^* = p_0^*$, $p = 0$) at both external boundaries in the supplementary material. At the proximal end of the vessel we impose homogeneous conditions on the cross-sectional area profile (zero slope) but apply this condition far enough upstream that it does not influence the solution.

In the next two subsections we will briefly outline the computational and analytical tools we use to study this system.

2.3 Computational methods

Numerically we solve Eqs. (5) and (6) in the elastic regions only (from which area and flux in the rigid regions can be inferred) using two complementary methods.

Our first method is a finite difference scheme based on semi-implicit time stepping (derived based on that used by [45, 46]). This scheme requires finite membrane tension, which has the advantage of allowing us to impose two extra boundary conditions on each region (so we can impose continuity of cross-sectional area explicitly between regions), but has the disadvantage that the membrane tension smooths the profiles so we never see multivalued solutions (*ie* shocks forming) and observe (short wavelength) dispersive oscillations near regions of large gradient in membrane area. Note that if this tension parameter is chosen sufficiently large ($\Gamma \gtrsim 10^{-2}$), then

it can suppress the propagating pressure fronts observed below. Further discussion of this method is provided in the supplementary material.

These dispersive waves are ameliorated with our second numerical method, a finite volume scheme based on that outlined in [15]. This method is based on a local Riemann solver at every time step and naturally facilitates discontinuities in the dependent variables; it therefore explicitly captures shock waves or elastic jumps. However, the method requires zero membrane tension, which lowers the order of our equations, reducing the number of boundary conditions that can be imposed. Thus, we only apply continuity of flux and pressure between regions, which allows abrupt changes in cross-sectional area at junctions. The method has a more stringent time step constraint (since it is fully explicit) which can make it computationally slow. This method also allows us to estimate the location the shock formation, where we assume a shock has formed when it has been identified by the Riemann solver at three neighbouring grid points. The point of shock formation is denoted $x = x_s$. Further discussion of this method is provided in the supplementary material.

Both numerical methods have their advantages and disadvantages (see further discussion in supplementary material) but we are reassured that the predictions are consistent (Sec. 3a).

2.4 Analytical method

To validate the results from these two numerical methods, we also construct an analytical solution based on a reduced form of our model. The full details of this solution are outlined in Appendix A but we will summarise the key details here.

We neglect region 4 entirely and assume regions 1 and 3 can be regarded as semi-infinite, as depicted in Fig. 1(c) with region 2 modelled as elastic (according to the constitutive law (6)) and of finite length L_2. We neglect membrane tension i.e. $\Gamma_{1,2,3} = 0$ and assume that perturbations from the base state are of small amplitude $\epsilon \ll 1$, to allow the governing equations to be linearised (variables denoted with a breve). This results in a constant (non-dimensional) wavespeed of disturbance $\breve{c}_j = \sqrt{v_0 k_j}$ $(j = 1, 2, 3)$, where v_0 is a constant determined by the tube law [29] in the form $v_0 = \mathcal{F}'(1)$, where prime denotes differentiation with respect to A. For example, $v_0 = 23/2$ for our tube law given in (6) with $m = 10$ and $n = 3/2$.

To facilitate an analytical approach we prescribe the external pressurisation of region 3, $\breve{p}_e(t)$, as a square wave applied over the time interval it takes for a disturbance to propagate along region 2 and be reflected back to source $(2L_2/\breve{c}_2)$. To reasonably compare to a particular numerical simulation we choose the amplitude of the analytical solution (ϵ) by imposing that the time-integrated external pressure is identical between the two approaches *ie* we equate the time integral over our approximation to external pressure in the analytical model (given by Eq. (A6)) to I_{tot}. Hence to compare to numerics carried out using external pressure profile (2), we take

$$\epsilon = \breve{A}_{\max} \equiv \max_{x,t}(\breve{A}(x,t)) = \frac{1}{L_2\sqrt{k_1 v_0}} I_{tot}. \tag{8}$$

The amplitude of this wavefront is thus inversely proportional to the length of region 2.

We solve for the cross-sectional area and flux profiles along each region and then focus on the limit of $k_2 \to \infty$ (an increasingly rigid intermediate region). In this limit our external pressure forcing tends to a delta function in time and the cross-sectional area profile in region 1 takes the

limiting form (see details in Appendix A)

$$A_1\left(x+\sqrt{v_0k_1}t\right)=\begin{cases}1+\breve{A}_{\max}e^{-2(x+\sqrt{v_0k_1}t)/L_2} & 0<x+\sqrt{v_0k_1}t,\ -\infty<x\leq 0\ t\geq 0\\ 0 & \text{otherwise}\end{cases}, \quad (9)$$

which decreases exponentially behind the advancing wavefront. Note that the exponent of this waveform is inversely proportional to the length of region 2. This prediction is plotted against numerical results in Fig. 3 below, showing excellent agreement particularly at small amplitude. We similarly obtain the cross-sectional area profile in region 3 in (23).

2.5 Energy partition

For a propagating disturbance we determine how energy is partitioned within any elastic region, which we use in Sec. 33.4. In particular, we calculate the energy equation within any region j ($j=1,2,3,4$) (assuming zero membrane tension, $\Gamma=0$) by taking the dot product of the momentum equation (5) with the velocity vector. To compute the total energy budget we integrate over the spatial domain. In particular, across region j with boundaries $L_{lj}\leq x<L_{rj}$ ($j=1,\cdots,4$), this gives four energy terms in the final energy partition which are denoted

$$\underbrace{\frac{\partial}{\partial t}\left(\int_{L_{lj}}^{L_{rj}}\left(\frac{1}{2}\frac{q^2}{A}\right)\,\mathrm{d}x\right)}_{\mathcal{K}_j(t)}+\underbrace{\int_{L_{lj}}^{L_{rj}}p\frac{\partial A}{\partial t}\mathrm{d}x}_{\mathcal{E}_j(t)}=\underbrace{\left[-qp\right]_{L_{lj}}^{L_{rj}}}_{\mathcal{P}_j(t)}+\underbrace{\left[-\frac{1}{2}\frac{q^3}{A^2}\right]_{L_{lj}}^{L_{rj}}}_{\mathcal{F}_j(t)}, \quad (10)$$

The two left-hand terms represent energy held within region j ($j=1,\cdots,4$): $\mathcal{K}_j(t)$ is the rate of change of kinetic energy in the fluid and $\mathcal{E}_j(t)$ is the rate at which energy stored in the elastic walls of the vessel. The right-hand terms represent energy entering and exiting the region, with $\mathcal{P}_j(t)$ representing the rate of working of pressure forces at the ends and $\mathcal{F}_j(t)$ representing the kinetic energy flux between the two ends of the region.

3 Results

In this section we predict the blood flow in the vessel in response to an acute rise in external CSF pressure external to region 3. Firstly, we consider the response to an external pressure forcing using numerical simulations and validate against the analytical model assuming the blood vessel is effectively rigid as it passes through the optic nerve (Sec. 33.1). We then focus particularly on the parameters pertinent the CRA and CRV in Sec. 33.2. In Sec. 33.3 we survey the parameter space. Finally, in Sec. 33.4 we examine why the confined region of the blood vessel (*ie* region 2) strongly influences the form of the response reaching the eye by considering a reduced model formed of just two regions of very different elastic stiffness. In all simulations we assume the elastic stiffness of regions 1 and 3 are identical (*ie* $k_1=k_3=1$) unless specified otherwise.

3.1 Vessel deformation after CSF pressure perturbation

In this section we model region 2 as entirely rigid. We relax this assumption in Sec. 33.4 to study the underlying mechanism of wave damping.

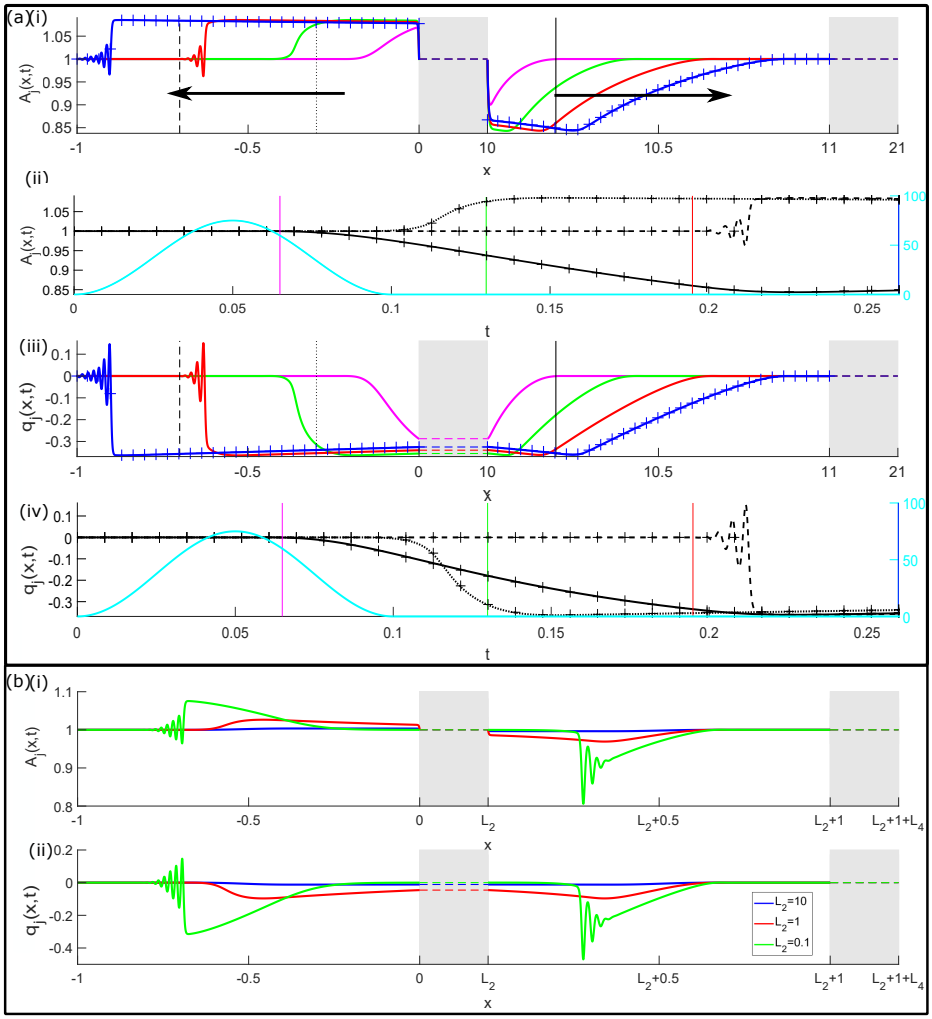

Figure 2: Response to a pressure perturbation (a) A baseline example for $L_2 = 10$ of amplitude $\Delta p = 75$ applied over $t_{ap} = 0.1$ (for the CRV this corresponds to $\Delta p^* = 3000\,\text{Pa} \simeq 23\text{mmHg}$ over a timescale of $t^*_{ap} = 0.5\text{ms}$) showing: (i) spatial profiles of the cross-sectional area along the vessel at four different times; (ii) time-traces of the cross-sectional area at three spatial locations; (iii) spatial profiles of the flux along the vessel at the same four times shown in (i) (crosses at the end time only); (iv) time traces of the flux at the same spatial locations as (ii). In each the solid lines are numerical results using the computational model with membrane tension while the crosses are the profiles using our shock capture method without tension. The vertical lines on the temporal plots illustrate the times the spatial profiles are plotted, while the vertical lines on the spatial plots illustrate the spatial locations where the time traces are plotted. The corresponding timetraces of the pressure profile are shown as the cyan curves in (a,i) and (a,iii) (corresponding to right hand axes). (b) Comparing the response for different L_2 including $L_2 = 10$ (blue), $L_2 = 1$ (red) and $L_2 = 0.1$ (green) for $\Delta p^* = 100\text{Pa}$ and $t^*_{ap} = 0.5\text{ms}$ showing spatial profiles along the vessel of: (i) cross-sectional area (ii) the flux. Other parameter values are listed in Tables 1 and 2. Note that in (i) and (iii) the x-axis values for distances as the rigid regions (with the grey background) are not to scale.

To examine the dynamic response to a large amplitude CSF pressure perturbation, in Fig. 2(a) we consider a perturbation of $\Delta p = 75$ applied externally to region 3 over a non-dimensional time interval $t_{ap} = 0.1$ (for the CRV this corresponds to a $\Delta p^* \approx 23$ mmHg over a dimensional time interval 0.5ms). Fig. 2(a) plots spatial profiles and time-traces of the vessel cross-sectional area (Fig. 2(a)(i,ii)) and axial flux (Fig. 2(a)(iii,iv)). We also plot the timetrace of the corresponding external pressure profile (Fig. 2(a)(i,iii). The solid lines are profiles obtained using the numerical method with finite membrane tension, while the crosses show the same profiles obtained using the shock-capturing numerical method without tension, demonstrating the consistency and close agreement between the two numerical methods. As expected, region 3 is constricted by the external pressure increase; due to the no flux boundary condition distal to the eye, fluid is forced proximally and so region 1 expands in response. However, the temporal profile in region 1 (Figs. 2(a)(ii,iv)) is significantly different to the prescribed CSF pressure profile: we observe a sharp increase in tube area at the front of the wave, where the maximal area expansion is observed, with a gradual decrease in tube cross-sectional area behind creating a long tail; this tail is significantly longer than the application time of external pressure and spatially it persists back to the junction between regions 1 and 2.

We also compute the Mach number of the flow to give an indication of the strength of the shock waves [30]. For the numerical example in Fig. 2(a), computed using the shock capture numerical method, we estimate $\overline{M} \approx 0.069$ in region 1 and $\overline{M} \approx 0.2208$ in region 3 (details on how this Mach number is calculated are given in the supplementary material).

To examine the role of the length of the blood vessel through the optic nerve (region 2), in Fig. 2b we consider the spatial evolution of the system for three values of L_2. Firstly, we notice that the response profile for smaller L_2 is significantly different to that described above. For $L_2 = 0.1$, we observe a single localised (propagating) pulse which is more similar to the time-trace in external pressure (compared to $L_2 = 10$). Additionally, we observe more significant steepening at the wave-front where (since we are assuming finite membrane tension) the system exhibits short wavelength dispersive waves. Similar dispersive waves are observed in our model of the optic nerve sheath [8]. In the absence of tension we expect (and indeed observe with our alternative numerical method) the system to form an elastic jump (or shock wave) with infinite gradient across the wave front. For $L = 0.1$ this elastic jump (or shock wave) also carries a much larger amplitude than for $L_2 = 10$. As L_2 increases the amplitude of the propagating wave-front decreases and the slopes at the leading edge become shallower. Despite the shallower slopes at the front for larger L_2, it can be shown that these fronts will eventually steepen to form a shock in the absence of membrane tension ($\Gamma = 0$), provided region 1 is sufficiently long. The distance propagated along region 1 before the formation of a shock is discussed in Sec. 33.3.

In the main text we consider no-flux proximal and distal boundary conditions. However, prescribed upstream and downstream pressure conditions are considered in the supplementary material. We find that these alternative boundary conditions make no difference to the profile in region 1 over the time interval of interest, although the dynamics in region 3 involves pressure waves propagating towards the interior from both ends, which will eventually interact.

We validate our predictions by comparing the full numerical model (the semi-implicit method with membrane tension) to our analytical model described in Sec. 22.4; we keep the timescale of the forcing short and ensure that the total external pressure per unit length along region 3, I_{tot}, is held constant between the models. The two approaches are compared in Fig. 3, where both show a propagating wavefront with a spatially decaying tail. For smaller L_2 the analytical model over-predicts the amplitude of the wave-front and exhibits lower propagation speeds, particularly when

the pressure disturbances are larger in magnitude (Fig. 3a). We attribute these differences to the absence of non-linear damping in the (linear) analytical model. The other significant difference is that the analytical model cannot capture wave steepening to form a shock. However, this analytic model elucidates the apparent difference in shape of the wave-fronts as L_2 increases (Fig. 3b): both profiles are exponential decaying behind the wave-front, but the decay is much less evident for larger L_2 as the decay rate is proportional to $1/L_2$ (9).

3.2 Comparing the central retinal artery and central retinal vein

The size and elastic properties of the central retinal vein and artery are different (see Table 1). To assess how these differences influence the response of the blood vessel within the eye (region 1), in Fig. 4 we examine the maximal amplitude of the waveform in region 1, denoted $A_{\max} = \max_{x,t}(A_1)$ (Fig. 4a), as well as the location where a shock is formed at the front of the wave, denoted x_s (Fig. 4b) as a function of driving pressure amplitude, Δp^*. As the artery has a considerably larger stiffness, the amplitude of the response is much lower than in the vein for the same external forcing (Fig. 4a). Additionally, a maximal external pressure of well over ten times larger is required for a shock to form in the artery at the same location as compared to the vein (Fig. 4b). For blood vessel rupture correlated to either the amplitude of the perturbation or to the gradient of the area profile (driven by the shock wave) this would indicate that the vein will be damaged for a much lower external forcing than the artery, consistent with physiological observations. Note also that we have included some simulations of the flow in the CRA using a different tube law in the online supplementary material, where the qualitative behaviour is similar to that reported here.

3.3 Shock formation in the retinal circulation

We investigate the role of model parameters on the response in region 1, focusing particularly on the amplitude and position of shock formation. In plots of wave amplitude we include predictions from both numerical models as well as the analytical model (ensuring I_{tot} is consistent between them). The results in Fig. 5 for both numerical models indicate only very minor differences between the two approaches, as expected.

To quantify the influence of increasing L_2, in Fig. 5(a) we again consider the maximal amplitude of the waveform in region 1 and the location where a shock is formed at the front of the wave. As L_2 increases the amplitude of the response in region 1 decreases (Fig. 2b). This is also evident in the analytic model, where the maximal deviation from the baseline cross-sectional area is inversely proportional to L_2 (8). Furthermore, we observe that increasing L_2 also increases the distance the waveform propagates along region 1 before forming a shock. Hence, longer region 2 delays shock formation. Such a prediction is interesting as the CRA and CRV bifurcate a short distance ($\approx$ 1mm) after entering the eye. Such a bifurcation would serve to weaken the propagating wave and so if the shock does not form before the first bifurcation it may not form at all.

To quantify the influence of increasing the baseline blood vessel stiffness, in Fig. 5(b) we show that increasing the stiffness of the blood vessel decreases the maximal cross-sectional area of the waveform in region 2, as expected. This can also be deduced from the analytic model (8), where the maximal amplitude of the response in region 1 is inversely proportional to $\sqrt{k_1}$.

To examine the influence of the total external pressure, in Fig. 5(c) we consider the maximal amplitude of the waveform in region 1 as a function of I_{tot}. Increasing Δp does not influence $A_{\max}$ provided we simultaneously decrease the timescale of the perturbation t_{ap} to ensure that

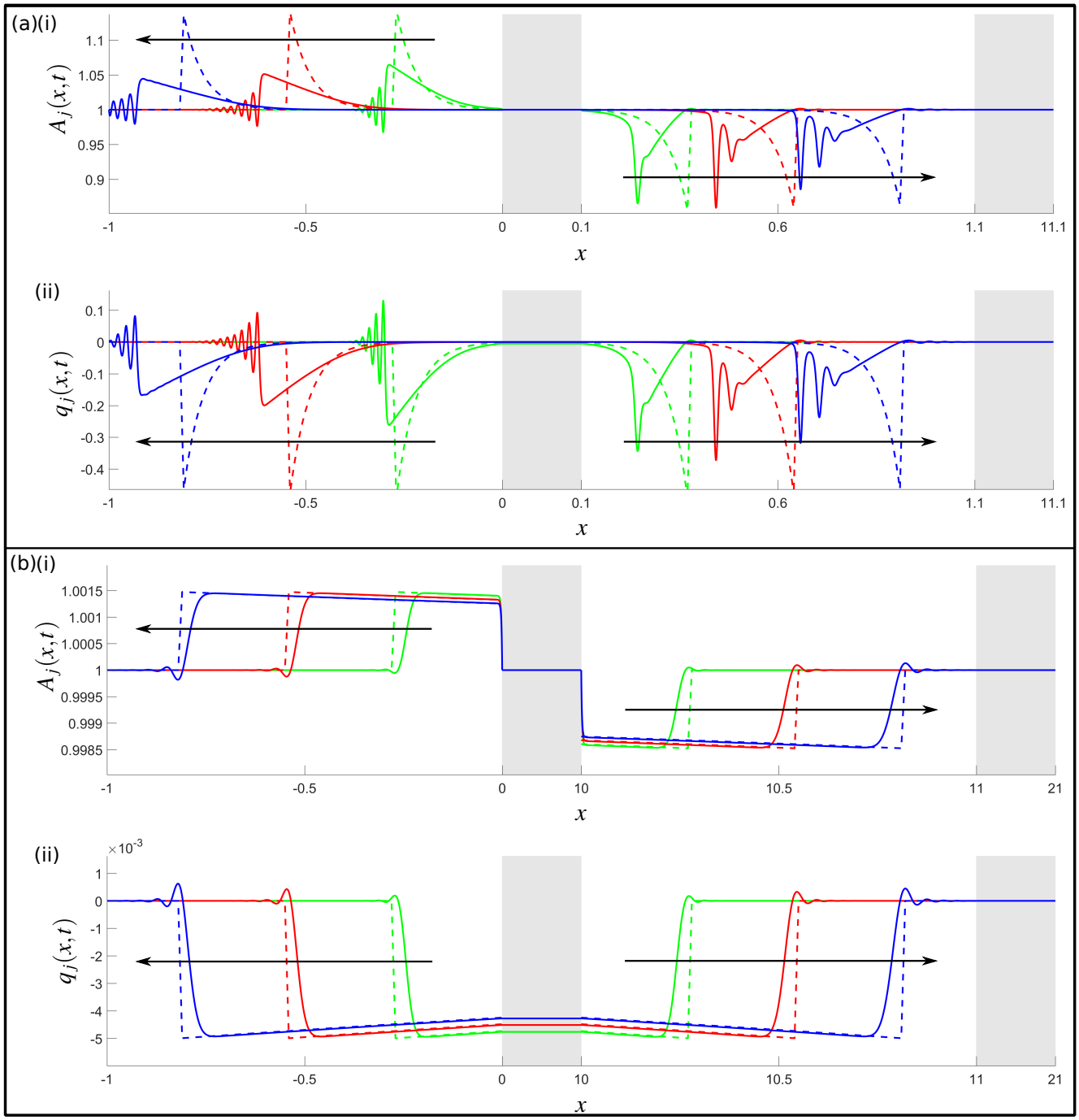

Figure 3: Response to a pressure perturbation of amplitude $\Delta p = 5$ applied over $t_{ap} = 0.02$ (for the CRV this corresponds to $\Delta p^* = 200\,\text{Pa} \simeq 1.5\text{mmHg}$ over a timescale of $t^*_{ap} = 0.1\text{ms}$) comparing predictions of the analytical (dashed lines) and numerical (solid lines) models for the same total imposed external pressure I_{tot} for (a) $L_2 = 0.1$; (b) $L_2 = 10$. In both cases we plot spatial profiles of (i) vessel cross-sectional area (ii) fluid flux at three different times. Here set $k_1 = 1$ and other parameter values are listed in Tables 1 and 2.

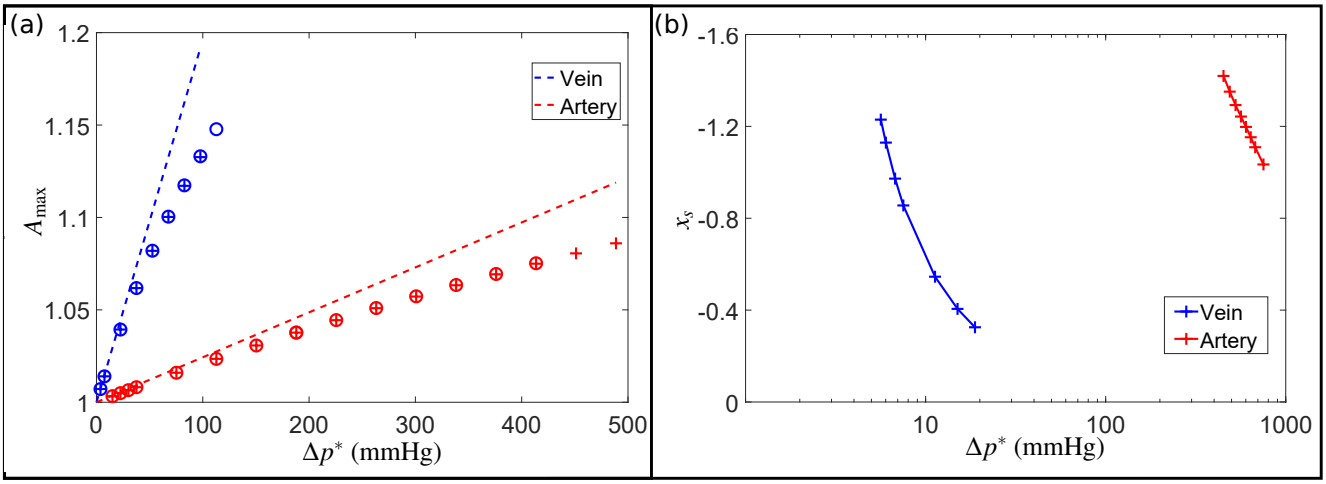

Figure 4: Comparing the response of the CRA (red) and CRV (blue) for $t^*_{ap} = 0.2$ms showing: (a) maximal amplitude of the tube cross-sectional area in region 1 computed using the numerical method with finite membrane tension (open circles), the shock-capturing numerical method without tension (crosses) and the analytical prediction (dashed line); (b) corresponding location of shock formation along region 1 (measured from $x = 0$). Here we set $k_1 = 1$ and other parameter values are listed in Tables 1 and 2.

.

I_{tot} remains constant (even at larger amplitudes where we may not expect linear theory to hold). This is consistent with the analytical model, where the amplitude of the waveform in region 1 is proportional to I_{tot}. Thus, a smaller pressure applied for a longer time can generate the same maximum amplitude as a larger pressure perturbation over a shorter time (though we do expect a larger perturbation applied over a short time to form a shock more quickly than the alternative). Conversely, increasing I_{tot} by increasing Δp for fixed t_{ap} we observe an increase in $A_{\max}$ (Fig. 5(c)(ii)), again in agreement with the analytical model.

3.4 Mechanism of protection

Our results have clearly identified the importance of region 2 (i.e. the region where the vessel is confined within the optic nerve) on the form of the response transmitted to the retinal circulation (region 1). To analyse why this intermediate region influences the response so significantly we now allow region 2 to be flexible and examine the limit as its stiffness increases (in the absence of membrane tension). In particular, we consider a reduced model comprised of only regions 1 and 2 (shown in Fig. 1(d)) where both have independent stiffnesses denoted k_1 and k_2, respectively, and the perturbation is applied as a pressure forcing in the fluid at the end of region 2 distal to the eye. We are interested in the limit $k_2 \gg k_1 = 1$ and use the shock capture numerical method.

To bound this reduced system we apply continuity of flux and pressure between the two regions and prescribe no flux at the end proximal to the eye. However, since the perturbation is progressing into undisturbed fluid we simply choose region 1 sufficiently long so that the wave-front never reaches the outlet (so this boundary condition does not affect the results).

To understand the fundamental differences as k_2 is increased we analyse the energy partition in

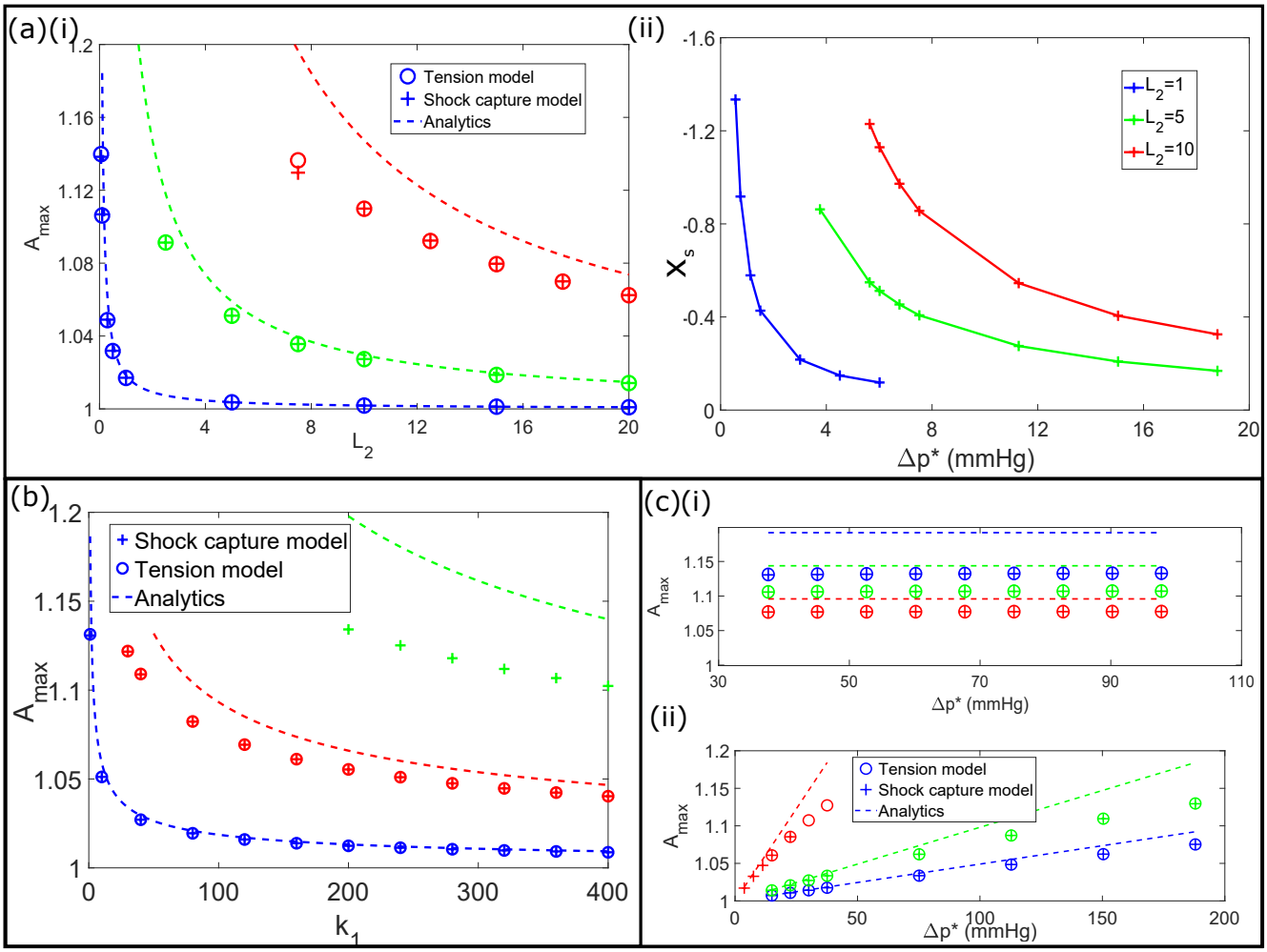

Figure 5: The influence of different parameters on the overall response. (a) Influence of increasing L_2 showing: (i) the maximal amplitude of the cross-sectional area in region 1 for $\Delta p = 12.67$ (blue), $\Delta p = 200$ (green) and $\Delta p = 1000$ (red) with $t_{ap} = 0.01$; (ii) location of shock formation in region 1 (measured from $x = 0$) for various Δp^* (assuming the parameter values of the CRV) with $t_{ap} = 0.04$ and $L_2 = 1$ (blue), $L_2 = 5$ (green) and $L_2 = 10$ (red). (b) The effect of increasing k_1 on maximal amplitude of the cross-sectional area in region 1, for pressure forcing of amplitude $\Delta p = 50$ (blue), $\Delta p = 250$ (red) and $\Delta p = 753$ (green) applied over $t_{ap} = 0.04$; (c) The effect of varying the external pressure forcing on the maximal amplitude of the cross-sectional area in region 1: (i) increasing Δp^* (assuming the parameter values of the CRV) for constant I_{tot}, where $I_{tot} = 26$ (blue), $I_{tot} = 19.5$ (green) and $I_{tot} = 13$ (red); (ii) increasing Δp^* (assuming the parameter values of the CRV) for fixed $t_{ap} = 0.01$ and $L_2 = 10$ (blue), $L_2 = 5$ (green) and $L_2 = 1$ (red). Here set $k_1 = 1$ (apart from (c)) and other parameter values are listed in Tables 1 and 2.

region 2 using (10), described in Sec. 22.5. For our system, the kinetic energy flux $\mathcal{F}_2$ is negligible since there is no mean flow. In the left-hand panels of Fig. 6, the distribution of energy between the four energy terms within region 2 (normalised by the approximate maximum input energy, $\max(\mathcal{P}_2)$) is shown for increasing k_2, while the right-hand panels illustrate the waveform (in cross-sectional area) in region 1 for increasing k_2. We are particularly interested in the partition of energy stored within region 2 into kinetic ($\mathcal{K}_2$) and stored elastic energy ($\mathcal{E}_2$).

As the perturbation is applied it generates a waveform which propagates rapidly along region 2 until reaching the boundary with region 1. If $k_1 \neq k_2$, part of this wave is transmitted into region 1 while part is reflected back into region 2. The reflected wave travels back along region 2, encountering the site of perturbation where it is reflected again. Reflection is driven by the local boundary condition, where we impose zero pressure after the initial pressure forcing has been fully applied. The re-reflected wave then propagates back along region 2 to the boundary with region 1, where it is again partially reflected and transmitted.

For low k_2 (Fig. 6(a) left-hand panel), separate stages are visible: the external pressure injects energy into the system and as the wave propagates along region 2 the energy is partitioned equally between $\mathcal{K}_2$ and $\mathcal{E}_2$ (see Sec. S.4 of the supplementary material). As the wave is reflected the energy partition changes, with a greater proportion transformed into kinetic energy ($\mathcal{K}_2$) while the total energy in region 2 drops since part of the wave is transmitted into region 1. As the wave is reflected back along region 2 the energy is once again equally partitioned between $\mathcal{K}_2$ and $\mathcal{E}_2$. Repetition of this process for multiple propagation/reflection cycles leads to spatially separated pulses transmitted into region 1 of decreasing amplitude but of comparable width.

Increases in k_2 result in increased wavespeeds along the region, so eventually the propagating wave is always in contact with one of the two ends: this results in a greater proportion of energy being transformed into kinetic energy (Fig. 6b) and the pulses transmitted into region 1 are no longer spatially separated. Hence, as $k_2 \to \infty$ a continuous disturbance arises in region 1 consisting of an initial pressure jump with a long tail, consistent with Fig. 2(a).

4 Discussion

In this study we have considered a theoretical model for the transmission of shock waves along the central retinal blood vessels toward the eye, driven by an acute rise in the cerebrospinal fluid (CSF) pressure. We modelled each blood vessel as a long collapsible tube divided into four regions in series (see Fig. 1a); these four regions mimic the course of the vessels as they approach the eye, including where they cross the nerve sheath (region 3), where they enter the eye (region 1) with an intermediate region (region 2) where they are strongly confined within the optic nerve.

The model predicts that an externally applied pressure pulse on region 3 of the vessel will lead to a localised constriction of cross-sectional area and drive flow into other compliant regions of the vessel (since the fluid is incompressible). Assuming that flow cannot leave the system (mimicking the closing of venous outflow as part of the injury), this leads to expansion of the vessel in the eye since typically this is where the vessel is least constrained; this expansion takes the form of a rapidly propagating pressure wave, which we have described using a combination of numerical and analytical approaches. In particular, our reduced model has elucidated that the pressure waveform within the eye is formed by superposition of waves which propagate rapidly back and forth along the constrained region of the vessel (see Fig. 6). Furthermore, the spatial decay of the composite profile behind the wavefront is inversely proportional to the length of this constrained section of

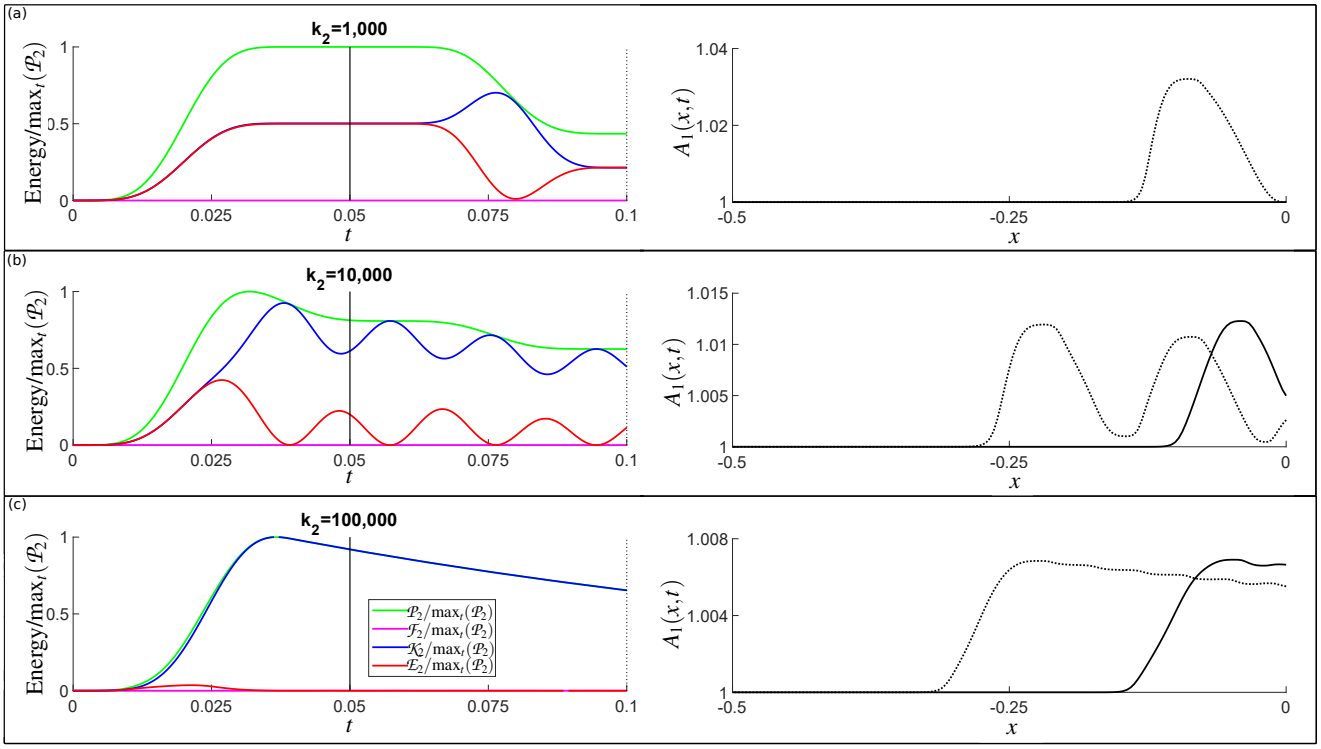

Figure 6: The influence of increasing the stiffness of region 2 in the two-region model for a pressure perturbation of amplitude $\Delta p = 1.333$ over a timescale of $t_{ap} = 0.04$: (a) $k_2 = 10^3$; (b) $k_2 = 10^4$; (c) $k_2 = 10^5$. The left hand panels show how the components of energy in region 2 are distributed (defined in Eq. (10) including $\mathcal{P}_2$ (green), $\mathcal{F}_2$ (magenta), $\mathcal{K}_2$ (blue) and $\mathcal{E}_2$ (red), each normalised by $\max(\mathcal{P}_2)$; right hand panels show the perturbation shape in region 1 at the two non-dimensional times marked by vertical lines on the left hand panels. Here set $k_1 = 1$.

the vessel (see Fig. 2,3 and Eq. 9). This implies that in normal physiology, where the length of the vessel segment through the optic nerve is typically 10 times longer than the region across the CSF space, this geometry of these vessels is significantly reducing the amplitude of any pressure waves entering the eye and effectively protecting the eye from damage. Furthermore, natural variability in the geometry of these blood vessels across the population could make some individuals more prone to larger amplitude responses in the eye.

As the steepening pressure wave enters the retinal circulation we expect that it will spread through the bifurcating network (in a similar manner to pulse waves [29]), leading to large transmural pressures across the weaker vessels in the tree and possibly to their rupture: a retinal haemorrhage. However, exploration of elastic jumps propagating on networks and associated vessel rupture is deferred to future work.

This model contains a simplified description of the blood flow and the elasticity of the vessel wall. In particular, it neglects the influence of viscous effects in the fluid, assuming these to act on timescales significantly slower than the application time of the acute rise in ICP. However, in the supplementary material we present preliminary simulations of the system with a realistic Reynolds number showing that, although viscosity reduces the amplitude of the pressure wave in region 1 and increases the time and distance taken to form a shock, the mechanisms reported herein still apply with a steepening pressure wave transmitted towards the eye. The model also neglects the baseline fluid flow in the vessel as we expect the system to be strongly subcritical. Preliminary analysis for small amplitude waves indicates that the base flow makes no quantitative difference to the predictions described above. The model neglects azimuthal flows and non-axis-symmetric buckling, where the mechanics of the vessel wall has been reduced to a 'tube-law' relationship between pressure and cross-sectional area. However, despite these limitations the model retains the essential physics required to exhibit wave propagation and wave steeping, as well as the formation of elastic jumps (shock waves).

The predictions of the model are also sensitive to the choice of membrane tension. As the tension parameter increases the lengthscale of the transmitted pressure perturbation expands across the eye compartment, eventually inhibiting the shock front (see supplementary material). In the physiological system this tension could depend on factors such as externally applied stresses, growth-induced remodelling or collagen fibre reinforcement of the vessel wall, and could be a source of pathological predisposition to a shock-induced eye damage.

Our model assumes that the system only feels the abrupt changes in the brain through an increase in CSF pressure external to region 3. However, these changes in the brain may be felt in other ways. For example, in Sec. S.3 of the supplementary material we modify the analytical model of Sec. 2(d) to suppose that some fraction of the external pressure increase is also applied to region 2, mimicking compression of the optic nerve. In this case we observe little difference to the predicted waveform in region 1, but note that nonlinear effects could lead to a greater difference. The perturbations applied in this model involve extremely large external pressures. Such large fluctuations could induce a number of additional effects such as changes in blood vessel material properties, abrupt temperature increases as well as formation of cavitation bubbles and acoustic waves. Investigation of such effects is deferred to future work.

Data Accessibility This article has no experimental data. Numerical scripts were written in Matlab 2018a and can be accessed at http://dx.doi.org/10.5525/gla.researchdata.795

Author's contributions TAS carried out the numerical and analytical analysis and drafted the manuscript; PSS conceived and coordinated the study, contributed to developing the numerical codes and edited the manuscript. All authors gave final approval for publication.

Competing interests We have no competing interests.

Funding TAS and PSS acknowledge funding from EPSRC grant no. EP/P024270/1 and PSS acknowledges support from EPSRC grant no. EP/N014642/1

Acknowledgements We would like to thank Dr Richard Bonshek (Manchester Royal Eye Hospital), Prof. Alex Foss (Nottingham University Hospital Trust), Prof. Phil Luthert (University College London) and Prof. Gary Misson (Aston University) for useful discussions on the clinical relevance of this work. We would also thank Dr. Bindi Brook (University of Nottingham) for providing and discussing her original shock capture code from which our shock capture model is adapted.

A Analytical Model

Here we outline the details of the analytical model introduced in Sec. 22.4.

In our model shown in Fig. 1(b), region 4 and the upstream end of region 1 have minimal effect on the wave form seen numerically. We neglect these from our analytical model and consider a semi-infinite region 1 ($-\infty < x \leq 0$), an intermediate region 2 of length L_2 ($0 \leq x \leq L_2$) but with finite stiffness k_2 (where $k_2 \to \infty$ is the limit of this region being rigid) and a semi-infinite region 3 ($L_2 \leq x < \infty$). The schematic of this model is given in Fig. 1(c). This formulation leaves L_2 as the only region length in the problem, so we could in principle scale lengths based on L_2 and thus reduce the number of parameters further. However, for ease of comparison with the numerical model we will maintain the same non-dimensionalisation used throughout the rest of the paper. We apply a pressure forcing $\breve{p}_e$ across the entire exterior of channel 3. However, despite applying this external pressure over an infinite domain this assumption still only inputs a finite amount of energy into the system as the disturbance lengthscale is finite. This is evidenced by the energy partition (10) since the contributions to $\mathcal{P}_3$ and $\mathcal{E}_3$ remain finite as the cross-sectional area is undisturbed ahead of the wave front propagating out from $x = L_2$ at finite speed. For notational ease we write the dimensionless stiffness in region 3 as k_3, but note that $k_3 = 1$ according to our non-dimensionalisation.

Our governing equations in each region are Eqs. (5) and (6) in the absence of membrane tension. For simplicity we assume a small amplitude response in each region of magnitude $\epsilon \ll 1$. Hence, we linearise through the expansion

$$(A_j, q_j, p_j) = (1, 0, 0) + \epsilon(\breve{A}_j, \breve{q}_j, \breve{p}_j) + O(\epsilon^2), \qquad (j = 1, \cdots, 3). \tag{11}$$

In this linearised system disturbances propagate at a constant wavespeed and we define $v_0 = \mathcal{F}'(\breve{A} = 0)$. At $O(\epsilon)$, Eqs. (5) reduce to the wave equation with known general solution with $\breve{p}_j = k_j v_0 \breve{A}_j$ and

$$\breve{A}_j = \frac{1}{\sqrt{k_j v_0}} \left[f_j(x - \sqrt{k_j v_0}t) - g_j(x + \sqrt{k_j v_0}t) \right], \tag{12}$$

$$\breve{q}_j = f_j(x - \sqrt{k_j v_0}t) + g_j(x + \sqrt{k_j v_0}t). \tag{13}$$

If the external pressure increases uniformly across an (infinite) region then the internal fluid pressure will also increase uniformly but no fluid motion will be generated. Hence the system will only experience fluid motion around non-uniformities in the external pressure, such as the boundary between regions 2 and 3. Since regions 1 and 3 are semi-infinite we can neglect waves

propagating into the system from without. There are then two boundary conditions between region 1 and 2 in the form of conservation of flux and pressure in the form

$$\breve{p}_1(x=0,t)=\breve{p}_2(x=0,t), \quad \breve{q}_1(x=0,t)=\breve{q}_2(x=0,t); \tag{14}$$

similarly between region 2 and 3 but with an additional contribution from the external pressure forcing giving

$$\breve{p}_2(x=L_2,t)=\breve{p}_3(x=L_2,t)+\breve{p}_e(x=L_2,t), \qquad \breve{q}_2(x=L_2,t)=\breve{q}_3(x=L_2,t). \tag{15}$$

The form of the external pressure forcing is chosen as a square wave to make the problem analytically tractable, in the form

$$p_e=\begin{cases}\frac{1}{2}\sqrt{k_2k_1}v_0\epsilon & 0<t<t_1\\ 0 & \text{otherwise}\end{cases}, \tag{16}$$

where $t_1=2L_2/\sqrt{k_2v_0}$. The timescale of the external pressurisation is chosen as the time taken for the wave to propagate along region 2, be reflected and return to the point of disturbance. Thus, as $k_2\to\infty$ this forcing tends to a delta function but the total applied pressure remains constant and is related to the amplitude by $I_{tot}=\epsilon L_2\sqrt{k_1v_0}$.

Therefore, we have four boundary conditions (14-15) to determine the relative amplitudes of the four waves g_1, f_2, g_2, f_3. We define $K_{ij}=\sqrt{k_i/k_j}$ for $i,j=1,2,3$. Using (14) we write f_2 and g_2 in terms of g_1 in the form

$$f_2(-\phi)=\tfrac{1}{2}\left(1-K_{12}\right)g_1\left(K_{12}\,\phi\right), \qquad g_2(\phi)=\tfrac{1}{2}\left(1+K_{12}\right)g_1\left(K_{12}\,\phi\right), \tag{17}$$

where ϕ is a function argument. Finally, we use (15) to write f_3 in terms of g_2 and f_2 in the form

$$f_3(\phi)=f_2\left(L_2-K_{23}(L_2-\phi)\right)+g_2\left(L_2+K_{23}(L_2-\phi)\right), \tag{18}$$

and then we derive a closed form equation for $g_1(\eta)$ in the form

$$g_1\left(\eta\right)=\frac{\left(1-K_{32}\right)\left(1-K_{12}\right)}{\left(1+K_{32}\right)\left(1+K_{12}\right)}g_1\left(\eta-2K_{12}L_2\right)-\begin{cases}\frac{\sqrt{k_1v_0}}{(1+K_{32})(1+K_{12})} & L_2K_{12}<\eta<3L_2K_{12}\\ 0 & \text{otherwise}\end{cases}. \tag{19}$$

This equation is of the form $g_1(\eta)=\alpha g_1(\eta-\beta)+\Phi(\eta)$, for $\alpha\neq 0$ and $\beta\neq 0$ known constants and Φ a known function. Since g_1 is identically zero for large negative values of η (before the external forcing has been applied), Φ is a non-zero constant on the interval $\eta\in[\beta/2,3\beta/2)$, which determines $g_1(\eta)$ in that interval. Beyond this interval Φ is identically zero so the equation becomes $g_1(\eta)=\alpha g_1(\eta-\beta)$ for $\eta\in[3\beta/2,\infty)$ which defines $g_1(\eta)$ over the rest of the domain. Hence, $g_1(\eta)$ is a piecewise constant function over intervals of length β. The general solution to this geometric progression for $n(\zeta_1)\in\{\mathbb{N}\cup 0\}$ takes the form

$$g_1(\zeta_1) \quad = \quad \begin{cases}-\frac{\sqrt{k_1v_0}}{(1+K_{32})(1+K_{12})}\left[\frac{(1-K_{32})(1-K_{12})}{(1+K_{32})(1+K_{12})}\right]^n & L_2K_{12}(2n+1)<\zeta_1<L_2K_{12}(2n+3)\\ 0 & \text{otherwise}\end{cases}, \tag{20}$$

for $\zeta_1 = x + \sqrt{k_1 v_0}t$. This then defines f_2, g_2 and f_3 using Eqs. (17) and (18) respectively (not listed for brevity). In region 1 the perturbation cross-sectional area becomes (for $n \geq 0$)

$$\breve{A}_1(\zeta_1) = \begin{cases} \frac{1}{(1+K_{32})(1+K_{12})} \left[\frac{(1-K_{32})(1-K_{12})}{(1+K_{32})(1+K_{12})}\right]^n & L_2K_{12}(2n+1) < \zeta_1 < L_2K_{12}(2n+3) \\ 0 & \text{otherwise} \end{cases}. \tag{21}$$

Setting $k_1 = k_3 = 1$, in the limit $k_2 \to \infty$ we have

$$n = \left\lfloor \frac{\left(x + \sqrt{k_1 v_0}t\right)}{2L_2} K_{21} - \frac{1}{2} \right\rfloor, \tag{22}$$

where $\lfloor\ \rfloor$ denotes the floor function. We form a continuous approximation by removing the floor function and then use the asymptotic result $(1 - 1/s)^s \to e^{-1}$ as $s \to \infty$ to obtain (9) in the main text. Hence, the amplitude of the waveform in region 1 decays exponentially behind the wave-front as shown in Fig. 3. Using a similar argument, we calculate the area of the compressed vessel in region 3 as

$$\breve{A}_3(x - \sqrt{k_1 v_0}t) = \begin{cases} -e^{-\frac{2}{L_2}(L_2 - x + \sqrt{k_1 v_0}t)} & L_2 < x - \sqrt{k_1 v_0}t < \infty \\ 0 & \text{otherwise} \end{cases}. \tag{23}$$

References

[1] Aryan HE, Ghosheh FR, Jandial R, Levy ML. 2005 Retinal hemorrhage and pediatric brain injury: etiology and review of the literature. *J. Clin. Neurosci* **12**, 624–631.

[2] Harding B, Risdon RA, Krous HF. 2004 Shaken baby syndrome. *BMJ* **328**, 720–721.

[3] Richards PG, Bertocci GE, Bonshek RE *et al.* 2006 Shaken baby syndrome. *Archives of Disease in Childhood* **91**, 205–206.

[4] Tuerkheimer D. 2014 *Flawed convictions: "Shaken Baby Syndrome" and the Inertia of Injustice*. Oxford University Press.

[5] Gilkes M, Mann T. 1967 Fundi of battered babies. *The Lancet* **290**, 468–469.

[6] Clarke MP. 2009 Vitreoretinal traction is a major factor in causing the haemorrhagic retinopathy of abusive head injury? - No. *Eye* **23**, 1761–1763.

[7] Levin A. 2011 Eye injuries in child abuse. In *Child Abuse and Neglect* pp. 402–412. Elsevier.

[8] Bonshek R, Cowley S, Jensen O, Pearce P, Ravi A, Stewart P, Whittaker R, Zouache M Understanding patterns of haemorrhage in the eye. *Report on the 2014 UK Maths in Medicine Study Group available from* `https://www.nc3rs.org.uk/sites/default/files/documents/Maths/understanding_patterns_of_haemorrhage.pdf`.

[9] Singh S, Dass R. 1960a The central artery of the retina I. Origin and Course. *Br. J. Ophthalmol.* **44**, 193.

[10] Singh S, Dass R. 1960b The central artery of the retina II. A study of its distribution and anastomoses. *Br. J. Ophthalmol* **44**, 280.

[11] Hayreh SS. 1963 The central artery of the retina its role in the blood supply of the optic nerve.. *Br. J. Ophthalmol* **47**, 651.

[12] Stewart PS, Jensen OE, Foss AJE. 2014 A Theoretical Model to Allow Prediction of the CSF Pressure From Observations of the Retinal Venous Pulse. *Invest. Ophthalmol. Vis. Sci.* **55**, 6319.

[13] Stewart PS, Foss AJE. 2019 Self-excited oscillations in a collapsible channel with applications to retinal venous pulsation *The ANZIAM Journal*, to appear

[14] Cowley SJ. 1982 Elastic jumps on fluid-filled elastic tubes. *J. Fluid Mech.* **116**, 459–473.

[15] Brook BS, Falle SAEG, Pedley TJ. 1999 Numerical solutions for unsteady gravity-driven flows in collapsible tubes: evolution and roll-wave instability of a steady state. *J. Fluid Mech.* **396**, 223–256.

[16] Igra O, X. W, Falcovitz J, Meguro T, Takayama K, Heilig W. 2001 Experimental and theoretical study of shock wave propagation through double-bend ducts. *J Fluid Mech* **437**, 255–282.

[17] Whitham GB. 1974 *Linear and nonlinear waves*. John Wiley & Sons Inc.

[18] Siviglia A, Toffolon M. 2013 Steady analysis of transcritical flows in collapsible tubes with discontinuous mechanical properties: implications for arteries and veins. *J. Fluid Mech.* **736**, 195–215.

[19] Siviglia A, Toffolon M. 2014 Multiple states for flow through a collapsible tube with discontinuities. *J. Fluid Mech.* **761**, 105–122.

[20] Woollatt D. 1965 An approximate theory for the transmission and reflection of simple waves at area changes and junctions in pipes. *Int. J. Mech. Sci.* **7**, 777–783.

[21] Davies P, Dwyer M. 1964 A simple theory for pressure pulses in exhaust systems. *Proc. Inst. Mech. Eng.* **179**, 365–394.

[22] Garhofer G, Werkmeister R, Dragostinoff N, Schmetterer L. 2012 Retinal blood flow in healthy young subjects. *Invest. Ophthalmol. Vis. Sci.* **53**, 698–703.

[23] Shapiro A. 1977 Steady flow in collapsible tubes. *J. Biomech. Engng.* **99**, 126–147.

[24] Ockendon H, Ockendon J. 2004 *Waves and compressible flow*. Springer.

[25] Cancelli C, Pedley T. 1985 A separated-flow model for collapsible-tube oscillations. *J. Fluid Mech.* **157**, 375–404.

[26] Halpern D, Naire S, Jensen O, Gaver D. 2005 Unsteady bubble propagation in a flexible channel: predictions of a viscous stick-slip instability. *J. Fluid Mech.* **528**, 53–86.

[27] Band L, Hall C, Richardson G, Jensen O, Siggers J, Foss A. 2009 Intracellular flow in optic nerve axons: a mechanism for cell death in glaucoma. *Invest. Ophthalmol. Vis. Sci.* **50**, 3750–3758.

[28] Love A. 1944 *A treatise on the mathematical theory of elasticity*. Cambridge University Press.

[29] Pedley TJ. 1980 *The fluid mechanics of large blood vessels*. Cambridge University Press.

[30] Chapman CJ. 2000 *High speed flow*. Cambridge University Press.

[31] Kotliar K, Hanssen H, Eberhardt K *et al.*2013 Retinal Pulse Wave Velocity in Young Male Normotensive and Mildly Hypertensive Subjects. *Microcirculation* **20**, 405–415.

[32] Kotliar KE, Lanzl IM, Hanssen H *et al.*2012 Does Increased Blood Pressure Rather Than Aging Influence Retinal Pulse Wave Velocity?. *Invest. Ophthalmol. Vis. Sci* **53**, 2119.

[33] Li Q, Li L, Fan S *et al.* 2017 Retinal pulse wave velocity measurement using spectral-domain optical coherence tomography. *Journal of Biophotonics* **11**, e201700163.

[34] Kotliar KE, Baumann M, Vilser W, Lanzl IM. 2011 Pulse wave velocity in retinal arteries of healthy volunteers. *Br. J. Ophthalmol* **95**, 675–679.

[35] Morgan WH, Yu DY, Balaratnasingam C 2008 The role of cerebrospinal fluid pressure in glaucoma pathophysiology: the dark side of the optic disc. *J. Glaucoma*, 17(5):408–413.

[36] Spahr H, Hillmann D, Hain C *et al.*2015 Imaging pulse wave propagation in human retinal vessels using full-field swept-source optical coherence tomography. *Opt. Lett.* **40**, 4771–4774.

[37] Spahr H, Hillmann D, Pfaffle C, Huttmann G. 2017 Comment on 'Retinal pulse wave velocity measurement using spectral-domain optical coherence tomography'. *J. Biophotonics*. e201700347 jbio.201700347.

[38] Olufsen MS. 1999 Structured tree outflow condition for blood flow in larger systemic arteries. *Am. J Physiol.* **276**, H257–H268.

[39] Westerhof N, Bosman F, De Vries CJ, Noordergraaf A. 1969 Analog studies of the human system arterial tree. *J. Biomechanics*. **2**, 121-134.

[40] Snyder RG. 1963 Human survivability of extreme impacts in free-fall. *Rep. Civ. Aeromed. Res. Inst. US*. Aug:1-29.

[41] Guidoboni G, Harris A, Cassani S *et al.* 2014 Intraocular pressure, blood pressure, and retinal blood flow autoregulation: a mathematical model to clarify their relationship and clinical relevance. *Invest. Ophthalmol. Vis. Sci.* **55**, 4105–4118.

[42] Pries AR, Secomb TW, Gaehtgens P. 1998 Structural adaptation and stability of microvascular networks: theory and simulations. *Am. J. Physiol. Heart Circ. Physiol* **275**, H349–H360.

[43] Moghimi S, Hosseini H, Riddle J *et al.*2012 Measurement of Optic Disc Size and Rim Area with Spectral-Domain OCT and Scanning Laser Ophthalmoscopy. *Invest. Ophthalmol. Vis. Sci.* **53**, 4519.

[44] Xie X, Zhang X, Fu J *et al.*2013 Noninvasive intracranial pressure estimation by orbital subarachnoid space measurement: the Beijing Intracranial and Intraocular Pressure (iCOP) study. *Crit. Care* **17**, R162.

[45] Stewart P, Waters S, Jensen O. 2009 Local and global instabilities of flow in a flexible-walled channel. *Eur. J. Mech. B* **28**, 541–557.

[46] Stewart P. 2017 Instabilities in flexible channel flow with large external pressure. *J. Fluid Mech.* **825**, 922–960.

[47] Sherwin SJ, Franke V, Peiro J, Parker K. 2003 One-dimensional modelling of a vascular network in space-time variables. *J. Eng. Math* **47**, 217–250.